GCAGS JOURNAL
A Publication of the Gulf Coast Association of Geological Societies
www.gcags.org

MECHANICALLY-PARTITIONED DEFORMATION RELATED TO REACTIVATED OBLIQUE SLIP FAULTS, PECOS RIVER CANYON

Gordon Smith[1], Chris Zahm[2], and Charles Kerans[3]

[1]*BHP Billiton, 1360 Post Oak Blvd., Houston, Texas 77056, U.S.A.*

[2]*Bureau of Economic Geology, Jackson School of Geosciences, University of Texas at Austin, University Station, Box X, Austin, Texas 78713–8924, U.S.A.*

[3]*Department of Geological Sciences, University of Texas at Austin, 1 University Station C1100, Austin, Texas 78712, U.S.A.*

ABSTRACT

Pre-existing structural elements can have profound effects on fracture and fault development in younger strata, especially in areas that undergo significant changes in tectonic setting due to reactivation along older structures. Increased fracture development around the faults may be difficult to detect in subsurface data, but highlights the volumetric extent of deformation within the fault damage zone and gives insight into the potential reservoir permeability impact faults may have in the subsurface. Observations of fracture style in outcrop can provide evidence of the conditions the fracture set developed within (e.g., extension, shear, or compressional). Moreover, fault-related fractures can vary in their intensity based on the mechanical properties of the host rock.

The focus of this study centers on the effects of potentially-reactivated Paleozoic faults along the Devils River Uplift on the development of faults and fractures in Cretaceous strata. Fault and fracture data were characterized in carbonate outcrop exposures with stratigraphic layers of varying mechanical properties. Additionally, this work inspects the impact of small faults on fracture development within variable strength strata as well as the role of mechanical stratigraphy on fault and fracture styles with specific attention given to the effect of diagenetic fabrics on fracture densities.

INTRODUCTION AND BACKGROUND

The extent of deformation associated with orogenic events is often defined by the last observed macroscopic compressional fold or fault at the foreland edge. This casual characterization misses critical penetrative strain (e.g., brittle faulting and fractures) that develops well into the foreland and may create high permeability fluid pathways that may be important to subsurface aquifers or reservoirs. Prediction of the magnitude, extent and orientation of faults and fractures within the foreland can be further complicated by the presence of older, pre-existing tectonic fabrics. The concept of penetrative strain is not new (Groshong, 1975; Mitra and Yonkee, 1985; Wojital, 1989; Hogan and Dunne, 2001; Burberry, 2015), and this paper documents fracture development in outcrop that we interpret to have been influenced by a legacy Paleozoic structure within the brittle deformation front of the Laramide Orogen. These observations are important to subsurface reservoirs because the zone that contains these exposures can be traced along the foreland front into the Eagle Ford Shale play of Maverick Basin.

Texas and northern Mexico have been subjected to a diverse suite of tectonic events, including the development of an extensive suture zone formed as a result of continent-continent collision during the Paleozoic Ouachita Orogeny (Flawn, 1961). Younger far-field compressional stresses reactivated these structures during the Late Cretaceous to Early Tertiary Laramide Orogeny creating a high concentration of small, en echelon faults in Upper Cretaceous strata known as the Carta Valley Fault Zone (Webster, 1980), which extends across the Devils River Uplift (Smith, 2013). The Devils River Uplift is an excellent location to explore the effects of reactivated pre-existing structures on secondary fault and fracture development in shallower strata. Previous studies have shown that when pre-existing fault planes are reactivated by horizontal compression, their displacement will have a component of strike or oblique-slip and the overlying strata may develop en echelon fault zones above the reactivated older structures (Tchalenko and Ambraseys, 1970; Moody and Hill, 1956; Wilcox et al., 1973). Numerous E, NE, and NW oriented faults were mapped using satellite imagery indicating a likely E–W pre-existing fault zone to be present in the region (Webster, 1980; Zahm and Kerans, 2010; Smith, 2013) (Fig. 1).

Manuscript received March 21, 2016; revised manuscript received June 13, 2016; manuscript accepted June 17, 2016.

GCAGS Journal, v. 5 (2016), p. 238–252.

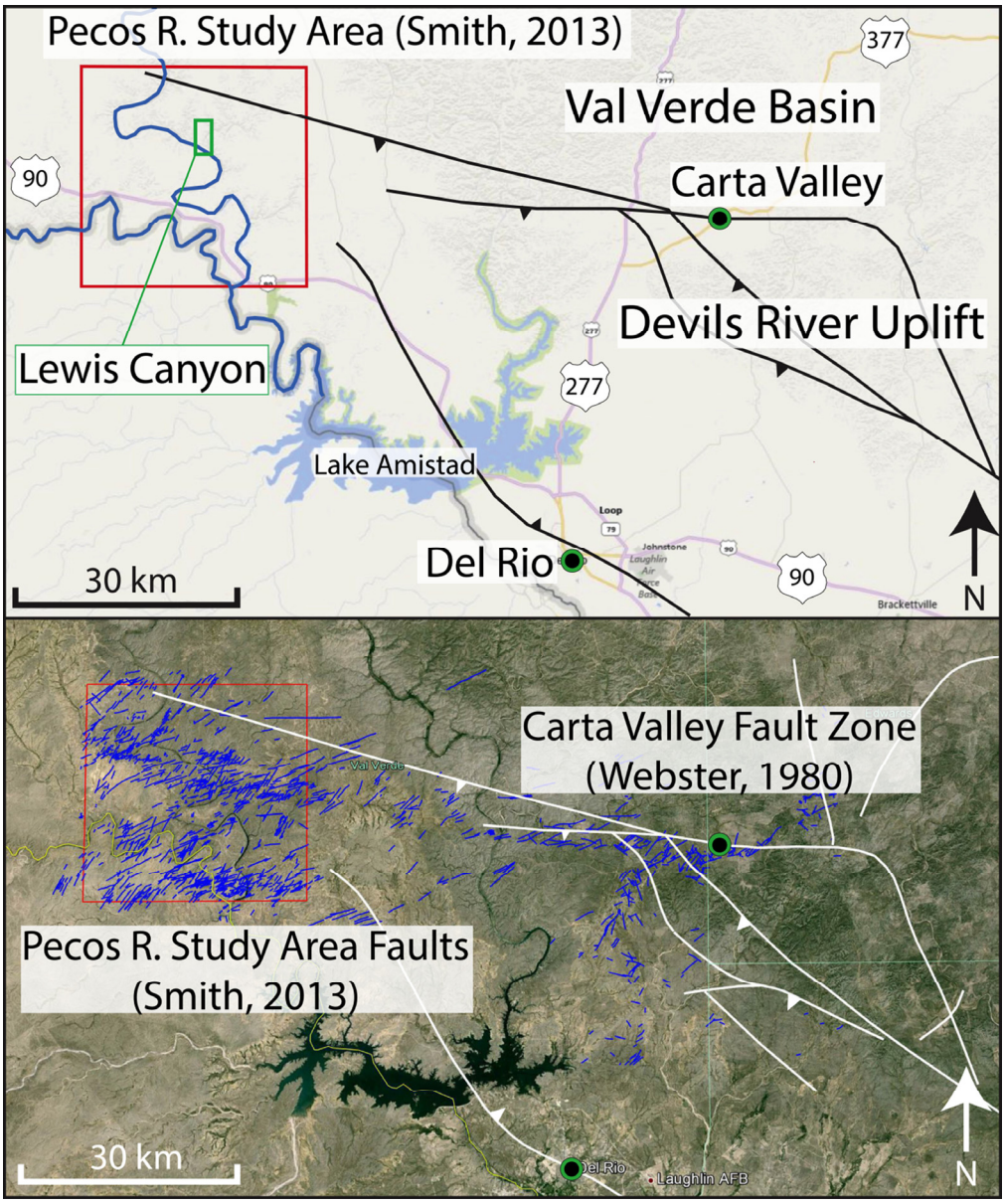

Figure 1. Pecos River study area (Smith, 2013) shown in relation to the Carta Valley Fault Zone (Webster, 2013). The Pecos River study area (1000 km^2) includes outcrops of platform and basin deposits associated with the Cretaceous Comanche Platform and Maverick Basin. Black (upper map) and white (lower map) lines show projected locations of subsurface faults associated with the frontal edge of the Ouachita Thrust Belt in southwestern Texas (Webster, 1980; Ewing, 1990).

The Pecos River Canyon exposes over 100 continuous km of Albian-age carbonate platform that directly overlies the Paleozoic Ouachitan Fold-Thrust Belt with associated E–W and SE–NW trending structures (Fig. 1). Geographically, the Pecos River Canyon sits in the northwest corner of a low-deformation regional plateau overlying the Devils River Uplift with a regional dip of less than 0.5 degrees to the southwest. Renowned for its remarkable continuity of time-correlative beds along more than 30 km of depositional dip, the lower Pecos River Canyon reveals a spectacular succession of Late Albian–age carbonate platform rocks (Kerans, 2002). Within the study area and at the surface, faults expressed in two predominant orientations of N38E and N70E are clustered in zones above the inferred subsurface structures (Zahm and Kerans, 2010; Smith, 2013) (Fig. 2). The faults form at predictable NE angles if the pre-existing structural fabrics associated with the Devils River Uplift are reactivated during left lateral oblique slip (Fig. 3). Smith (2013) interpreted satellite imagery from Google Earth and found well exposed structural lineaments and faults traces exposed in the sparsely vegetated the surface exposures west of the Carta Valley Fault Zone. In this study, more than 900 structural lineaments were mapped within in a 1000 km^2 study area encompassing the lower 100 km of the Pecos River (Fig. 1). Faults in this area are described as having minimal offset compared to trace length, near vertical dip, and some degree of dissolution collapse (Zahm and Kerans, 2010; Smith, 2013) similar to faults mapped by both Webster (1980) and Kastning (1983).

Documented subsurface examples of small en echelon fault development over pre-existing structures are rare. However, Smith (2013) documented a similar fault style within a large 3D seismic volume approximately 160 km southeast of Lewis Canyon within the Maverick Basin. Fault mapping and characterization revealed Late Triassic to Early Jurassic rift faults were identified as controlling structures for fault networks in the shallower Cretaceous section, which are time analogous to outcrops of the Pecos River Canyon (Scott, 2004). This study also demonstrated that mapped Cretaceous fault intensity increases over older Mesozoic structures and the shallow, younger en echelon faults were oriented approximately 30–45 degrees different than the older pre-existing faults. It is believed that the faults mapped in Pecos River Canyon are believed to have a similar genesis to structures in the Maverick Basin and likely formed during left-lateral oblique slip along the deeper pre-existing structures (Smith, 2013). While they are found in different localities above differ-

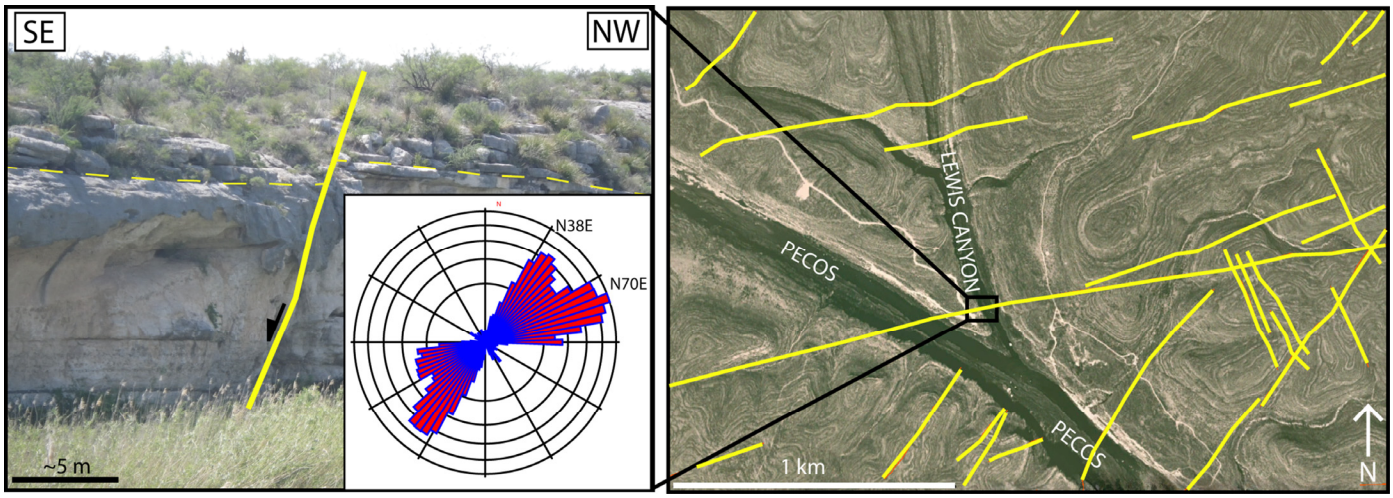

Figure 2. Fault traces mapped in Google Earth (right) contrasted with an outcrop photo (left) of a specific fault from the entrance to Lewis Canyon, which was originally mapped on satellite images. Length-weighted rose diagram shows orientations for more than 900 structural lineaments mapped from remote sensing images on Google Earth. The photographed fault has 2 m of offset and a trace length of 4 km.

Figure 3. Block diagram model of tectonic setting in Val Verde County showing oblique reactivation of pre-existing Paleozoic structures. The stratigraphy is modified after Nicholas and Rozendal's (1975) interpretation of Shell 1 Stewart well in Val Verde County, Texas.

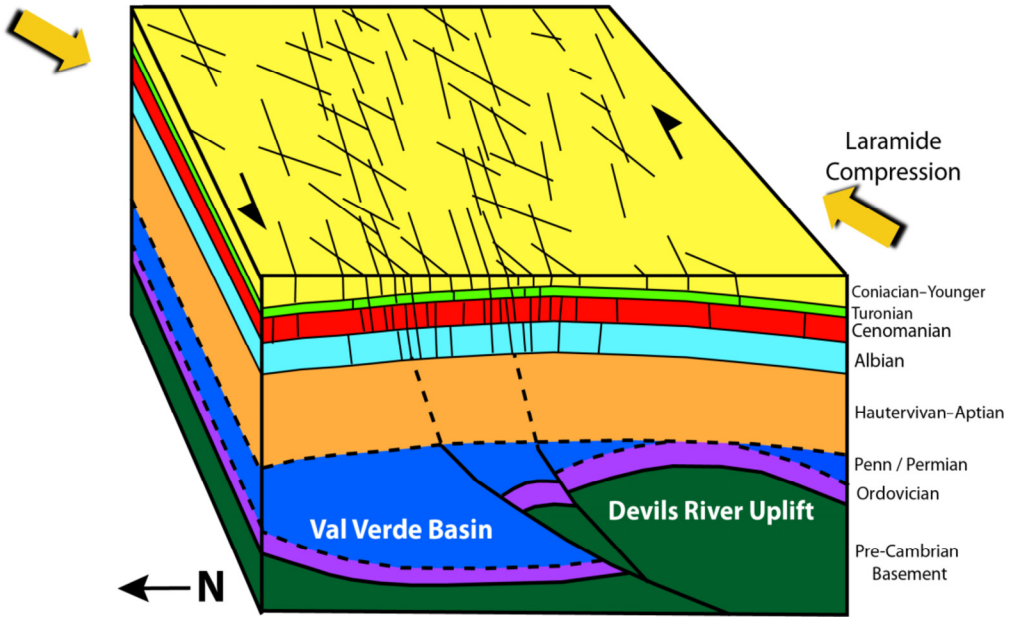

ent tectonic elements, these two fault networks exhibit comparable brittle deformation controlled by secondary movement of pre-existing structures.

Associated with each of the faults observed in satellite view are zones of increased fracture intensity as shown by Zahm and Kerans (2010) and Smith (2013). The degree of fracture development (I.e., fracture intensity) and distribution of fractures around exposed faults is variable owing to several factors including heterogeneity in rock strength or brittleness (Zahm et al., 2010; Agosta et al., 2010; Ferrill et al., 2011); degree of dolomitization (Ortega, 2010); lithologic facies (McGinnis et al., 2015); and relative thickness of interbedded of weak and brittle strata (Zahm et al., 2010). Each of these factors are plausible causes for increased or reduced fracture development near the fault zone and many are not mutually exclusive.

A goal of this work is to characterize the degree of fracture intensity associated with the small offsets faults within a vertical succession of layered carbonates to determine the degree of fracturing within units of varying strength. Mechanical partitioning, specifically how certain layers or packages can influence the local structural style, was evaluated within this exposure. This has important implications for petroleum basins where penetrative deformation in the form of small faults and fractures highlight the variability and extent of deformation of small fault damage zones and gives insight into the potential permeability impact faults may have in the subsurface.

METHODS

Detailed investigation of fracture development was conducted in Lewis Canyon, a dry side canyon along the Pecos River. Lewis Canyon contains outcrop exposures of the uppermost strata of the Albian 18 highstand systems tract and is characterized by high-energy skeletal grainstones and rudstones (Kerans, 2002) that have continuous exposure for 100s to 1000s of meters (Fig. 4). Ten consecutive carbonate layers, distinguishable by horizontal bedding planes, color changes, differences in mineralogy, and

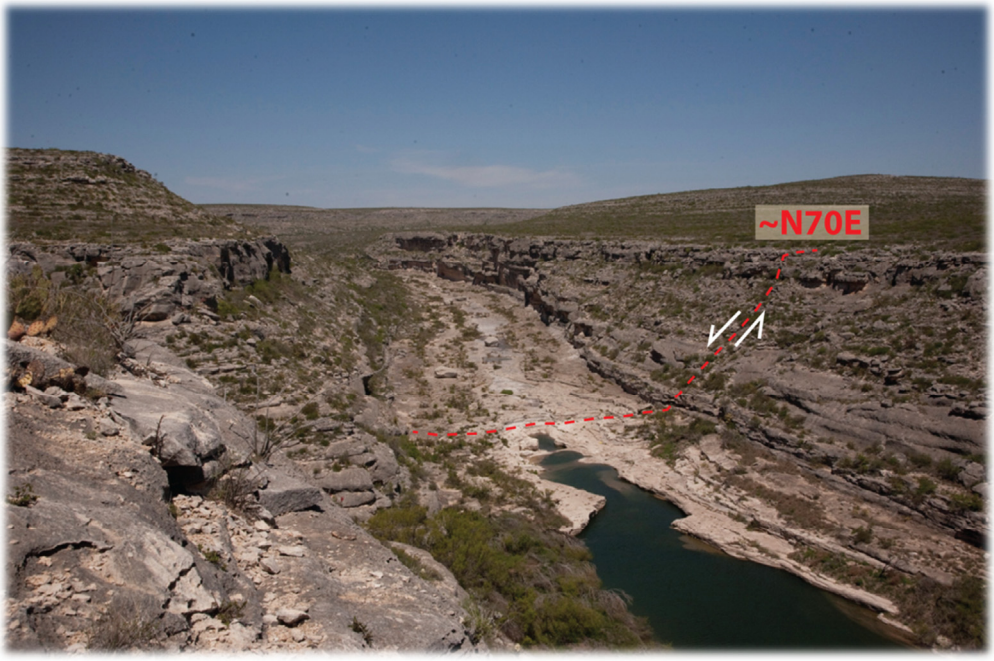

Figure 4. Photograph taken from the rim of Lewis Canyon (modified after Zahm and Kerans, 2010). Red dashed line indicates a fault trace mapped in outcrop.

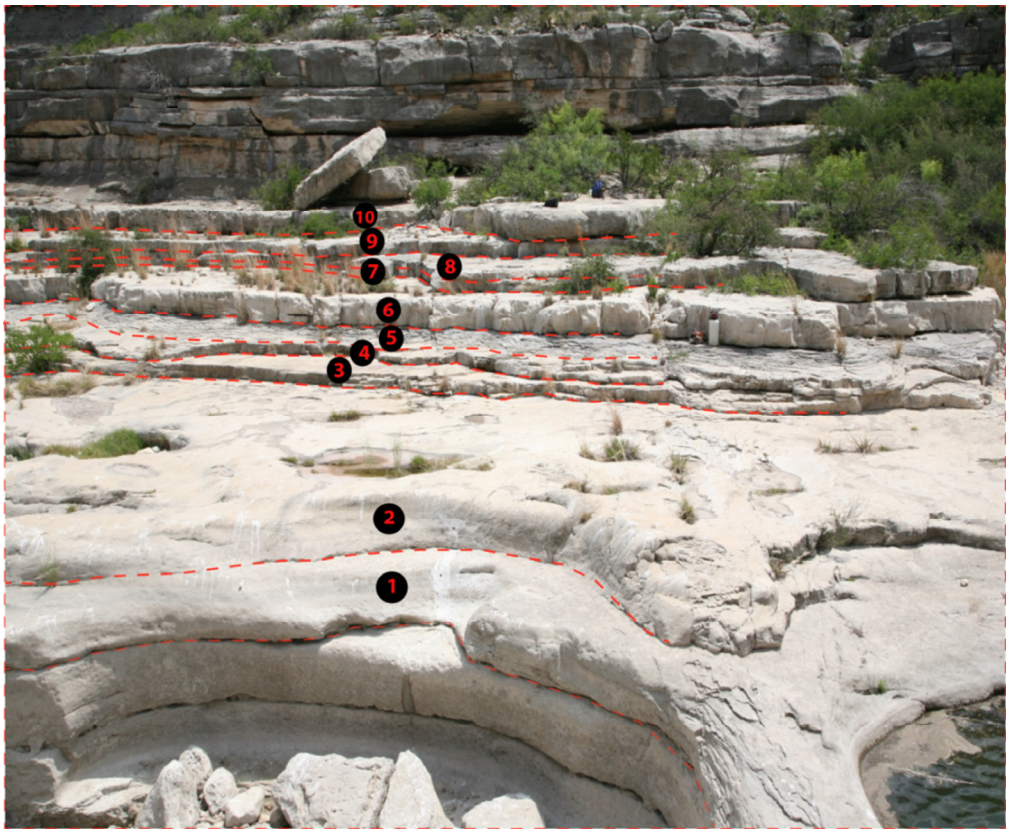

Figure 5. Locations where 10 individual layers were identified and core plugs were taken for creating thin sections. Location is near the water's edge in the mouth of Lewis Canyon.

differences in weathering profiles, were mapped around the water's edge near the canyon's mouth (Fig. 5). They have been designated as layers, and not beds, because some adjacent layers may be part of the same depositional bed but have been altered by diagenesis, resulting in multiple weathering profiles. These layers were hypothesized to act as different mechanical units containing different fracture populations that could be mapped, quantified, and compared.

Thin sections of core plugs taken from the 10 layers were analyzed using a petrographic microscope under 5x and 10x magnification. Additionally, a dye containing alizarin-red was applied to half of each thin section to differentiate between dolomite and calcite. Porosity for each layer was estimated using a pixel counting technique with digital photomicrographs. Because the impregnated epoxy is blue, image software was used to separate and count the blue pixels in any given photo so their percent-

age of the total image could be calculated and used as a proxy for porosity. Potential biases with this technique include pores below the resolution of the 5x and 10x images as well as a limited resolution of an image. The same technique was applied to each thin section to reduce the relative bias related to this method.

Using a handheld rebound Schmidt hammer, rock strength measurements were recorded for layers 1–10 using the methods described by Poole and Farmer (1980). Replicating the conversion process of Deere and Miller (1966), the rebound strength values were converted to unconfined compressive strength (UCS), which is a common unit used to interpret rock competence in Cretaceous strata (Zahm and Enderlin, 2010; Ferrill et al., 2011). Higher UCS values indicate higher strength rocks, which may fracture more readily than rocks with lower UCS values under similar stress conditions.

Fracture Characterization

High-resolution, GPS–located aerial photographs were taken of the 1.6 km pavement in Lewis Canyon using a quad-copter unmanned aerial vehicle (UAV). The photogrammetry company CameraWings was contracted to acquire the high-resolution orthogonal (i.e., down-looking) and oblique images of the canyon pavement and walls. Georeferencing of the manually placed control points allowed the stitching software (Agisoft Photostitch) to create a seamless photograph by creating i, j, and k normals of the photos (Zahm, 2013). This technique enables the development of 3D models via the use of photogrammetry. The result is a 1–3 cm resolution 2D geotiff and a 5–25 cm resolution 3D digital color model of the canyon pavement. Additionally, using QT Modeler software, a 3D digital elevation model (DEM) of the pavement was created to more accurately map the topographic boundaries between different layers of carbonate strata.

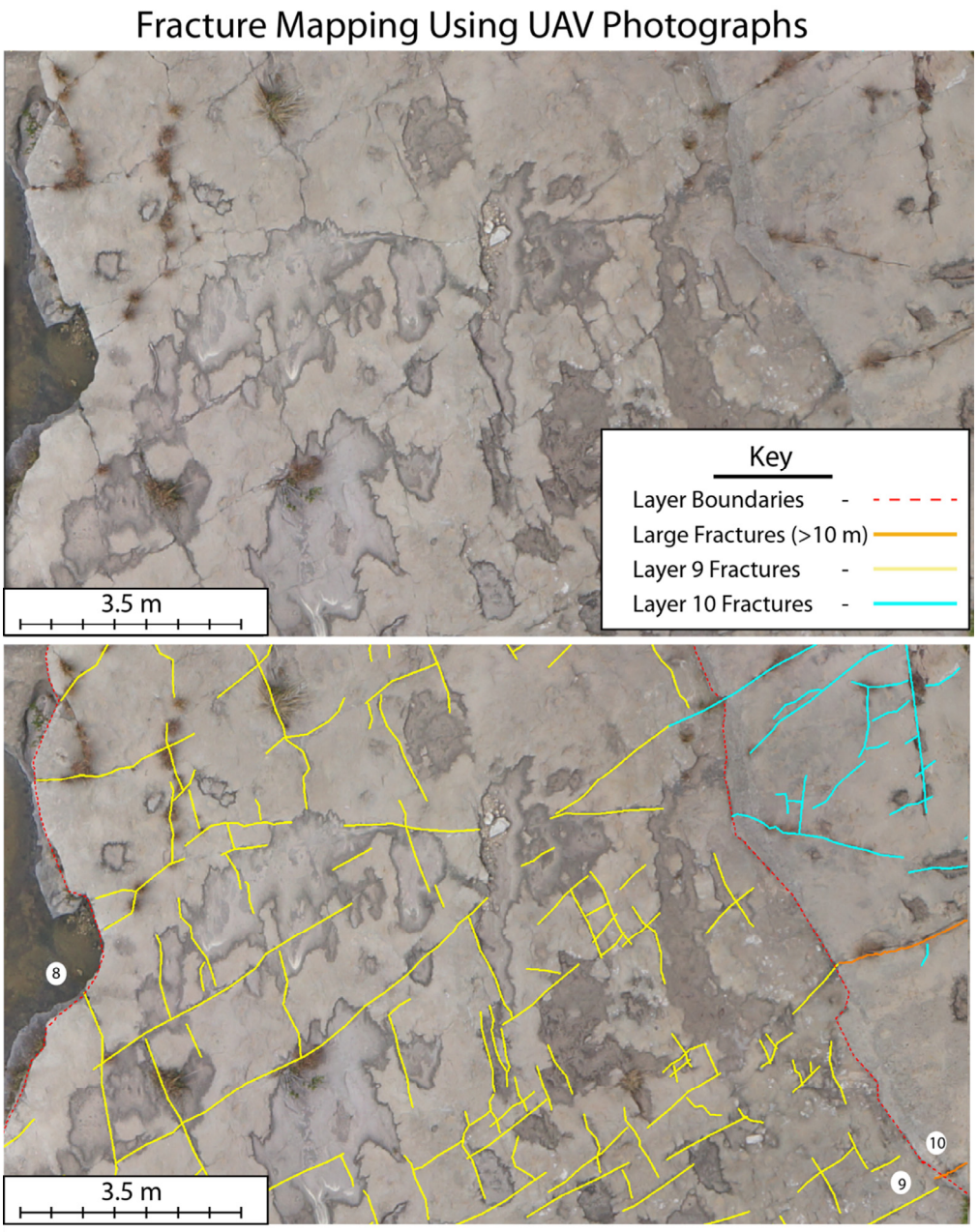

Figure 6. An original high-resolution photo acquired with an unmanned aerial vehicle (UAV) (top) is compared with the same image with fractures mapped by layer in using Global Mapper software (bottom). Fractures are commonly identified by differential weathering, which causes slight dissolution and color change along fracture traces.

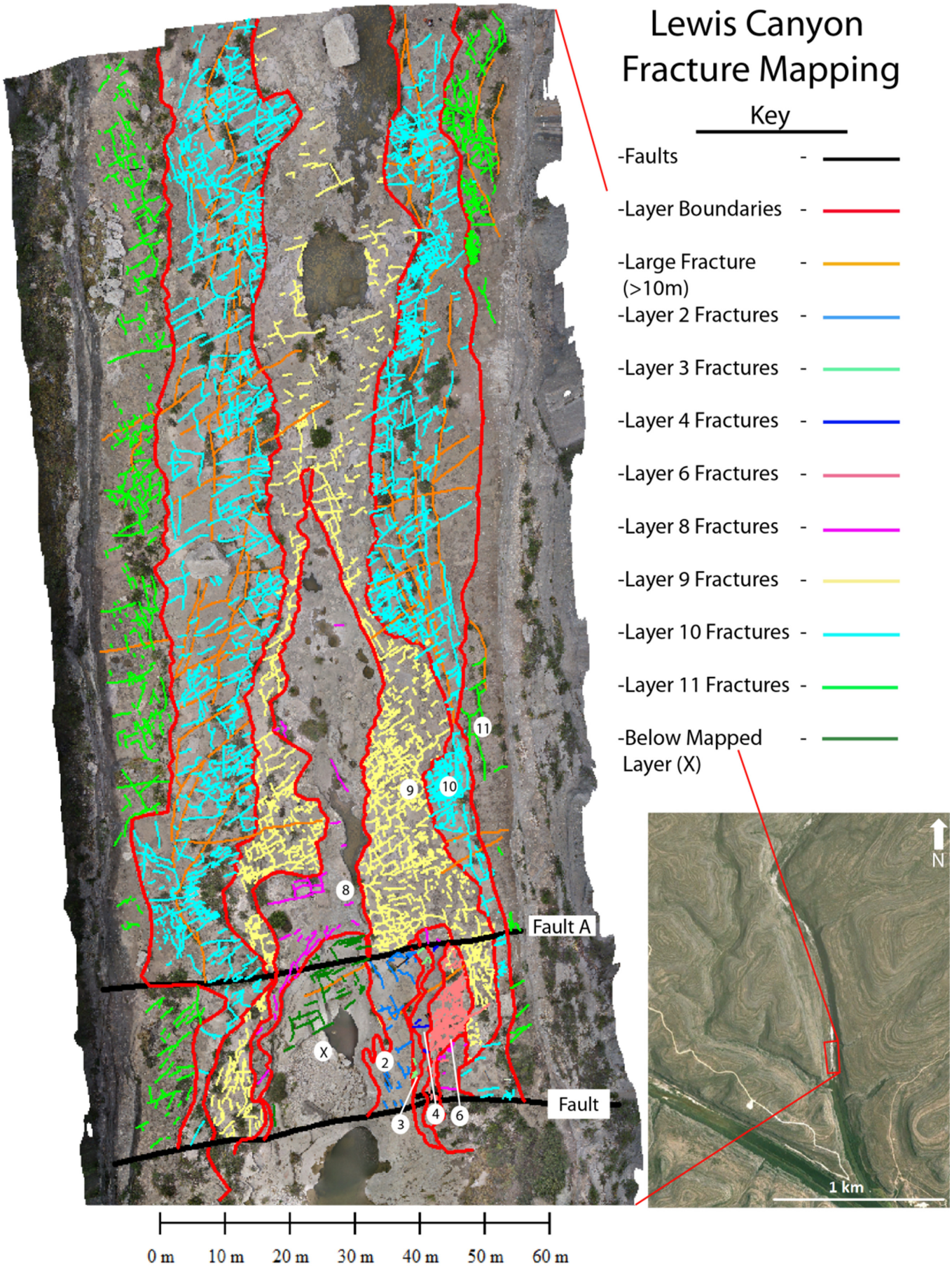

Figure 7. Lewis Canyon fractures by layer. Aerial image acquired via unmanned aerial vehicle (UAV).

Composite high-resolution Geotiffs of Lewis Canyon's floor with resolutions of 1–3 pixels/cm were evaluated in Global Mapper software. Fracture networks were digitally annotated for each layer that forms a visible pavement surface (Figs. 6 and 7). Layers 8–10 create prominent pavements to the north of fault A and were individually mapped to isolate the fracture data within each layer for comparison. Below the three prominent pavements, layers 2–4 and 6 display small pavements around the canyon mouth and were similarly mapped. The mapped fractures were analyzed for dominant orientation trends by creating length-weighted rose diagrams of fracture orientations. Specifically, diagrams were collated for four distinct fracture populations: total fractures, large fractures (i.e., greater than 10 m), fractures in prominent pavements (i.e., layers 8–10), and fractures in smaller pavements near the canyon mouth (i.e., layers 2–4 and 6). Additionally, to compare fracture orientations between individual layers, separate length-weighted rose diagrams were created for all pavement forming layers.

RESULTS

Thin sections revealed that layers 1–5 are limestone, and layers 6–10 are mostly dolomite (dolostone) (Figs. 8 and 9). Of the five dolomitized layers, layers 7 and 8 are completely dolomitized so that any depositional fabric or original grains were completely destroyed and replaced by dolomite crystals. Layers 6, 9, and 10 are fully dolomitized but retain some primary depositional fabric. Molds of leached bivalves and ostracods are visible in layers 6 and 9, whereas originally aragonitic caprinid fragments are observed in layer 10, and these have been filled by calcite cement. Porosities ranged from <1% to ~28%, with layers 7 and 8 having the highest porosities of 17% and 28%, respectively.

The 10 carbonate layers identified in Figure 5 have thicknesses between ~0.25 and 1.15 m. Their cumulative average UCS value, calculated from rock strength measurements taken with a Schmidt hammer, is 63 MPa. The UCS measurements for individual layers fall in a range of 60–70 MPa with one exception. Layer 8 has an average UCS of 49 MPa, a relatively low value inconsistent with the range of average UCS values displayed by the other nine layers. Layer 2 has the highest average UCS of 70 MPa (Table 1).

Fracture Styles and Measurements

One common fracture style observed in outcrop has subparallel, laterally stacked en echelon fractures oriented ~65° counterclockwise from a through-going shear zone, indicative of Riedel shears (Riedel, 1929; Tchalenko and Ambraseys, 1970; Wilcox et al., 1983). Other en echelon fractures are not stacked, but align laterally in steps in which fracture barely overlaps the previous one. Figure 10 shows an example with both of these fracture patterns in the same location. Additionally, there are many examples of separate fractures originally arranged in an en echelon pattern joining together into a single, larger fracture.

Small faults or fault splays near fault A display mosaic monomictic breccias in sub-linear traces as well as chaotic monomictic breccias expressed in irregular to sub-rounded forms along crude lineaments. Many fractures in Lewis Canyon are calcite cemented with < 2 mm of fill. Even with small widths, they can often be mapped in aerial photos due to differential weathering. Larger fractures, which are usually a linked set of smaller, previously separate fractures, were observed with widths between 0.2 and 5 cm. Connection points where fractures linked together in the past are usually the widest points in any given fracture trace.

More than 3,000 fractures mapped in Lewis Canyon from UAV photos reveal two predominant orientations; N55E and N25W (Fig. 11). The largest mapped fracture is 34.02 m long, and the smallest is 0.11 m. The average fracture length is 1.76 m with a standard deviation of 2.14 m (Fig. 12). Fractures greater than 10 m were classified as large fractures, and within the mapping area, they cluster into two orientations as well; N55E and N15E. Layers 8–11, which make up the bulk of the canyon pavement, have nearly identical dominant orientations to the entire fracture population, whereas layers 3, 4, and 6 near the water's edge cluster into dominant orientations of N65E and N25W. Most of the layer-specific rose diagrams are bimodal with varying fracture orientations (Fig. 13). Layers 1, 5, and 7 have no diagram because they are recessive and form no pavement surfaces. Conversely, layers 8–11 form the largest pavements, providing more robust datasets to assess their qualities.

Fracture intensity (length/area) was calculated for layers with observable pavement outcrops. Only layers 6, 9, and 10 have intensities above 0.4 m/m^2, and layer 6 has the highest fracture intensity of 1.9 m/m^2. Figure 7 shows that lower layers have limited data sets taken from relatively small pavements (i.e., layers 2–7), so intensity data calculated from these layers may be unknowingly skewed by local distortion. Especially problematic is that the smallest pavements sit adjacent to and in between fault A and another fault 20 m to the south. Observing fractures solely near the fault may skew fracture intensities higher than the regional value for these layers.

To observe spatial distribution and the potential control preexisting faults have on fractures in Lewis Canyon, fracture intensities within layers 8–11 were calculated in 10 m bands away from fault A. When each bin's intensity is plotted against the distance away from fault A in a scatter plot, changes in fracture intensity with respect to the fault is observed (Fig. 14). Linear trend lines of best fit are displayed on the scatter plot. Layers 8 and 9 both display linear trends that have decreasing fracture intensities away from the fault with coefficient of determination (R^2) values of 0.81 and 0.90, respectively. Layer 10 shows no conclusive trend and has an R^2 trend line value of 0.04.

DISCUSSION

En echelon fracture styles are created by shear stress along a controlling plane (Tchalenko and Ambraseys, 1970; Wilcox et al., 1973). These zones are evidence of the same shearing process that created regional high-intensity fault zones during the reactivation of subsurface Paleozoic structures and form similar relative geometries on a smaller scale. While fractures in outcrop are observed to mimic the regional fault trend, they are controlled locally by faults (e.g., fault A) whose primary slip induced shear in the surrounding area, causing fracturing. However, local faults formation was likely controlled by deeper pre-existing structures so the genesis of local fracturing is inherently sequential.

Locally, small induced shear zones create sub-parallel fractures that link together to form observable lineaments. Given enough time or enough stress, fractures within these shear zones will link into larger fractures and eventually become small faults. Indeed, it was observed in outcrop that as en echelon fractures begin to connect, they will slip and brecciate (Fig. 15). In Lewis Canyon fractures oriented ~N55E are either the most dominant or second most dominant orientation in each of the 11 mapped layers, except in layer 8 (Fig. 13). These fractures are interpreted to be synthetic fractures formed from shearing on fault A and/or the fault ~25 m further south. Both faults display brecciation, but their offsets are difficult to quantify because the host rock is laterally indistinctive. These faults strike ~N80E and are likely synthetic shears themselves with respect to movement on preexisting Ouachita orogenic structures. As synthetic shears to subsurface structures, these faults would have small components of left-lateral slip. The dominant local fracture orientation of ~N55E is 25° counter clockwise from N80E and that places them in the range of orientations for synthetic structures in shear models (Fig. 16).

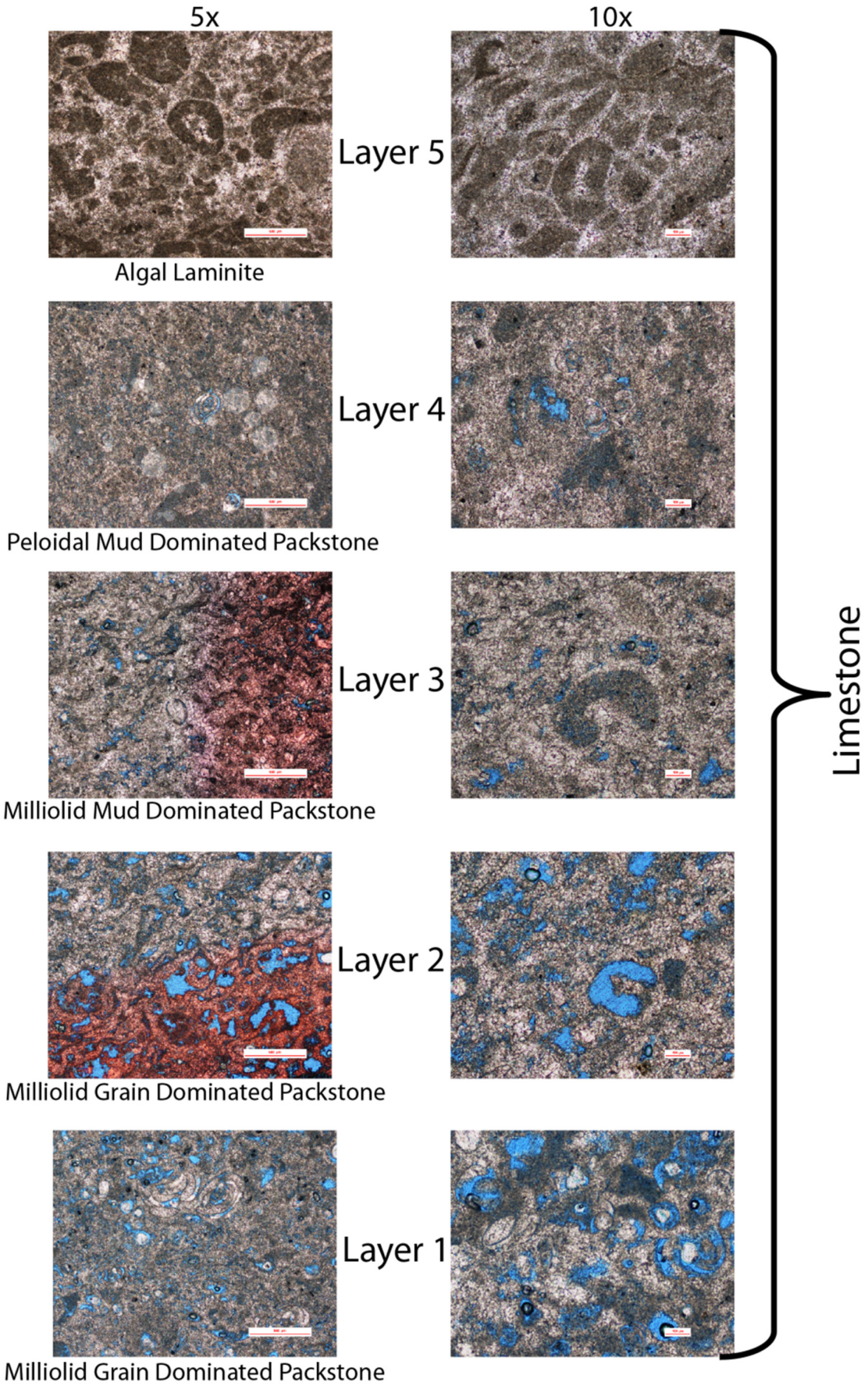

Figure 8. Photomicrographs of layers 1–5. All were stained by the alizarin red–S, indicating that they are limestone. Staining effects are seen in images of layers 2 and 3.

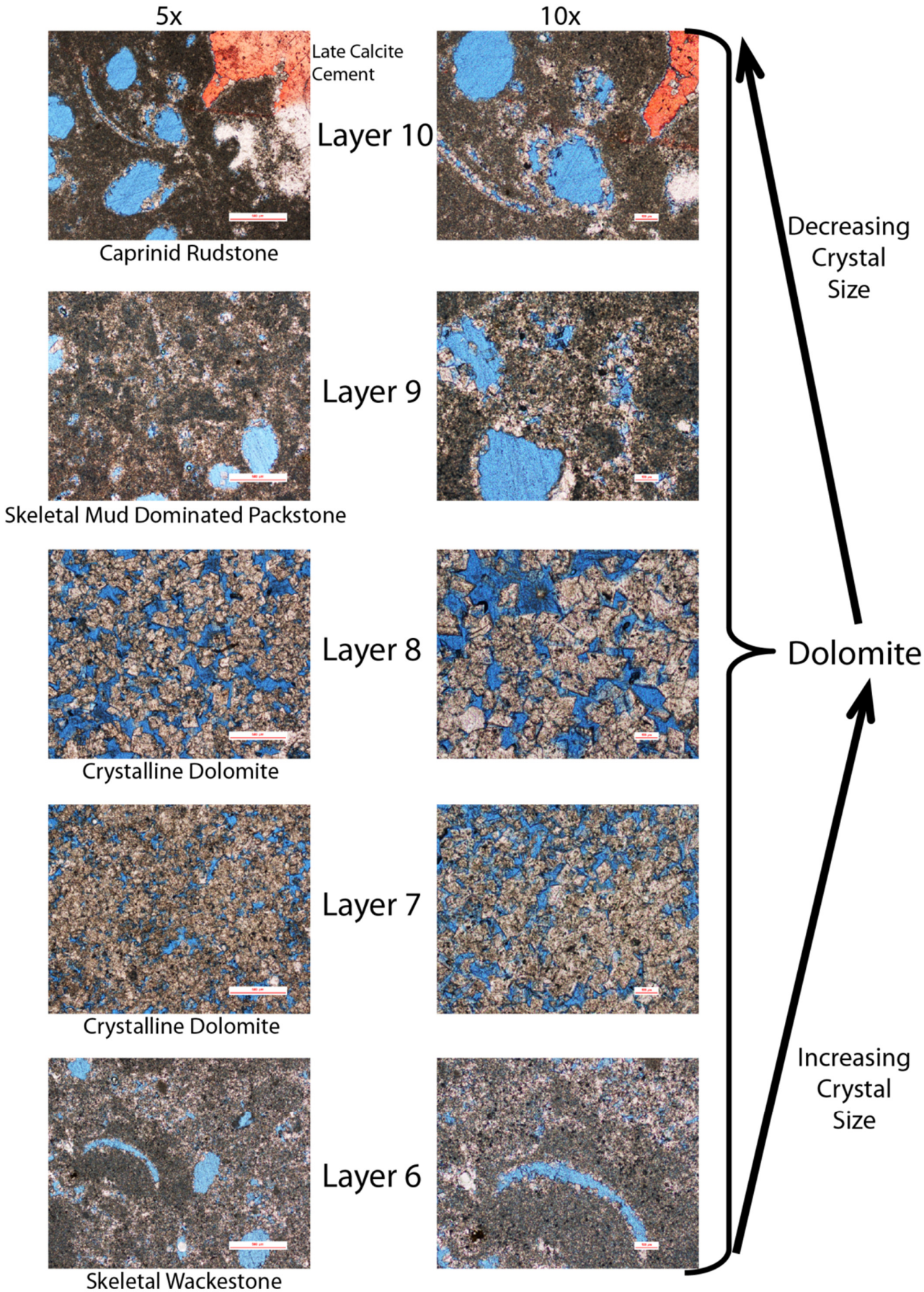

Figure 9. Photomicrographs of layers 6–10. These layers are all mostly dolomite with the exception of late calcite cement in layer 10.

Table 1. Unconfined compressive strength (UCS) of the 10 layers mapped in Lewis Canyon. Measurements taken in outcrop with a Schmidt hammer. Approximately 10 measurements were taken for each layer and then averaged.

Unconfined Compressive Strength in Lewis Canyon		
Layer	**Average UCS (MPa)**	**UCS (MPa) Range**
1	61.5	53–67
2	69.5	67–72
3	66.8	64–74
4	64.1	54–71
5	66.0	57–74
6	66.5	64–67
7	65.8	61–71
8	48.7	41–56
9	60.5	57–63
10	63.1	59–71

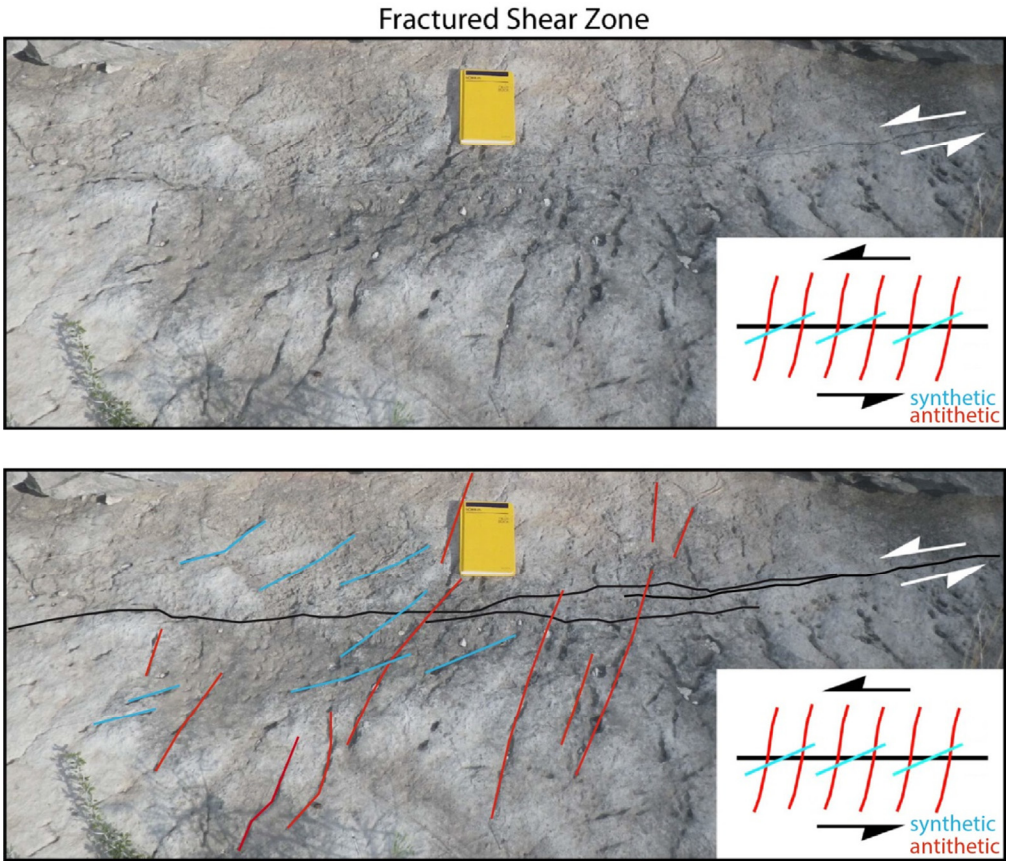

Figure 10. Outcrop photo of a left-lateral shear zone with synthetic and antithetic fractures.

The second most common orientations are N15W–N25W. These fractures form roughly orthogonal to the dominant fracture orientations and are commonly observed in outcrop to abut NE trending fractures as well as link longer NE fractures together. The origin of these fractures is difficult to discern, but the most plausible interpretation is that they represent a secondary fracturing event that occurred during regional uplift of the Terrell Arch (Sellards et al., 1933; Freeman, 1961). Sellards et al. (1933) postulated that this uplift is the source of local thinning in the Del Rio Formation, and Zahm and Kerans (2007) suggested that NW fractures mapped in a different locality within the Pecos River Canyon may be associated with outer-arc extension of this arch. Kastning (1983) suggested that the reason for a lack of NW oriented caves in the Langtry area is that Laramide compression effectively closed any NW oriented structures, which discouraged fluid flow and cave development.

Limited numbers of fractures greater than 10 m in length are found throughout the pavement, mostly in layers 9 and 10. These fractures have two strong orientations of N55E and N15E (Fig. 11). The N15E petal is part of a wider cluster of substantial petals between ~N20W–N20E. This concentration of fracture orientations, centered around due north, is not a dominant trend in the overall fracture pattern. These large fractures are here proposed to be a result of the anisotropic stress field around the vertical pavement boundaries of layer 9 and 10. These fractures form parallel to these boundaries, which reflect the N–S canyon trend. Layer boundaries are expressed as vertical breaks or "stair stepping" edges where the layer is essentially truncated. Because

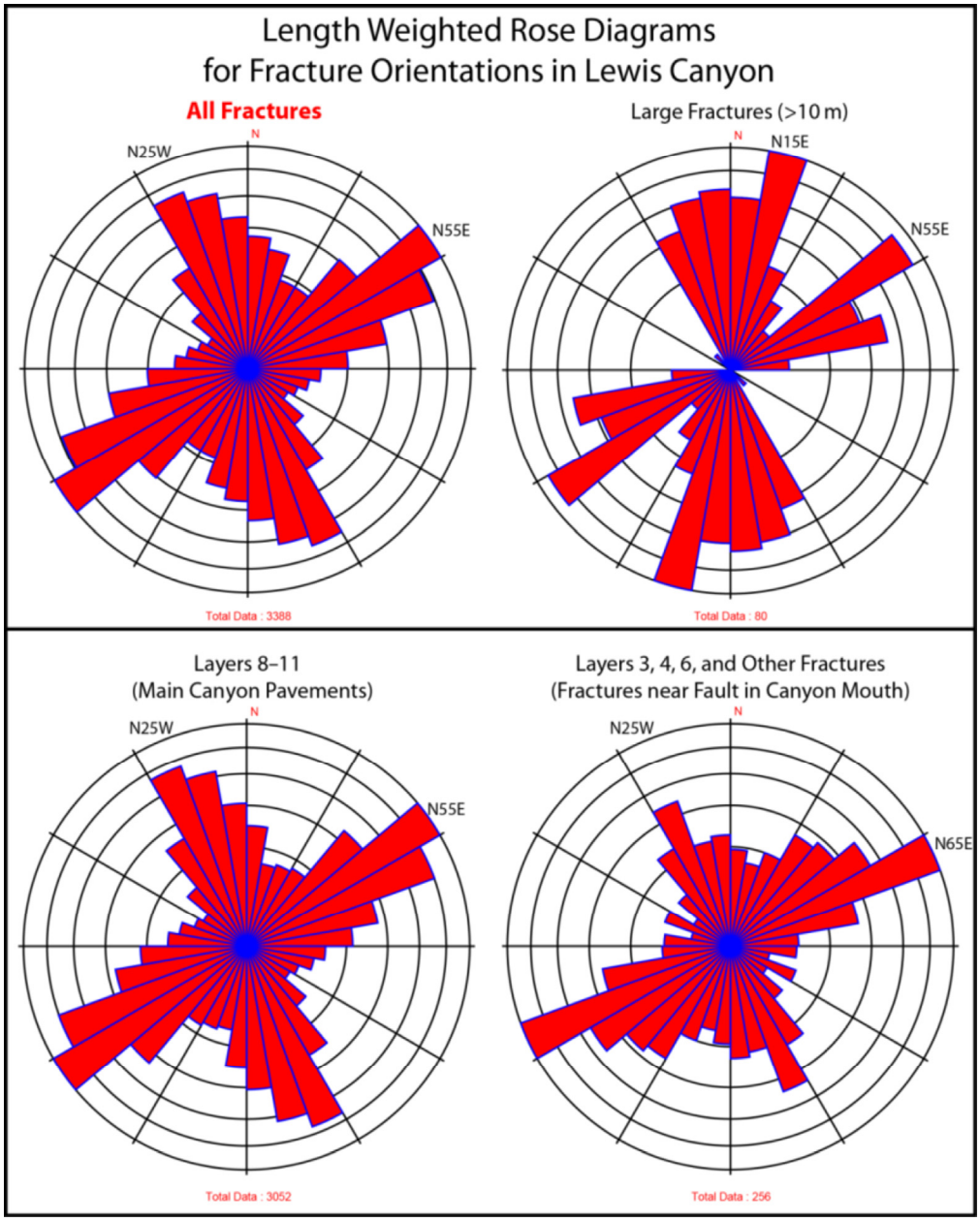

Figure 11. Length-weighted rose diagrams for Lewis Canyon fractures.

there is no compressional force perpendicular to the truncated boundaries, fractures are likely to form parallel to and near their edges. Enhanced weathering around the exposed layer boundaries enhances and enlarges these fractures.

Fracture intensities of layers 2–4 and 6 were calculated from relatively small pavement areas, and when compared with layers 8–10 are considered less accurate measurements. For this reason, only layers 8–10, which all form prominent pavement surfaces in the study area, are considered for fracture intensity comparison. Of these three, layers 9 and 10 have similar fracture intensity values of 0.55 and 0.68 m/m^2, respectively. Layer 8 has a much lower intensity of 0.1 m/m^2. This locally abnormal fracture intensity is corroborated by the significantly lower average UCS value measured in layer 8. Additionally, petrographic analysis reveals that layer 8 has unique characteristics that may contribute to its low fracture intensity, specifically its relatively high degree of dolomitization. A combination of increased porosity and larger dolomite crystal size may decrease the competence of layer 8.

Fracture intensity varies both between layers and spatially with respect to faults. Intensity decreases linearly away from fault A in layers 8 and 9 whereas there is a weak or inconclusive decreasing linear correlation in layer 10 (Fig. 14). These data confirm that movement along faults is a partial control for the fracture distribution in Lewis Canyon. Zahm and Kerans (2010) also documented fault damage zones with decreasing fracture intensities away from a controlling fault in slightly younger strata within a nearby canyon wall in Lewis Canyon. The results of their work and this study document that fracture intensity commonly decreases away from faults, with specific rates being dependent on the mechanical properties of any given layer. Fault damage zones documented by Caine et al. (1996), Augosta and Aydin (2006), and McGinnis et al. (2015) display similar patterns of fracture intensity increasing around faults (i.e., fracture halos). Enhanced fracture porosity and permeability is likely found in fault halos described by this study and Zahm and Kerans (2010).

There is a potential sampling bias regarding the contacts between layers 8–10. These boundaries have sharp terminations, creating vertical steps. Higher fracture intensities are commonly observed within ~5 m of the vertical layer terminations. These apparent high densities are interpreted to be the results of in-

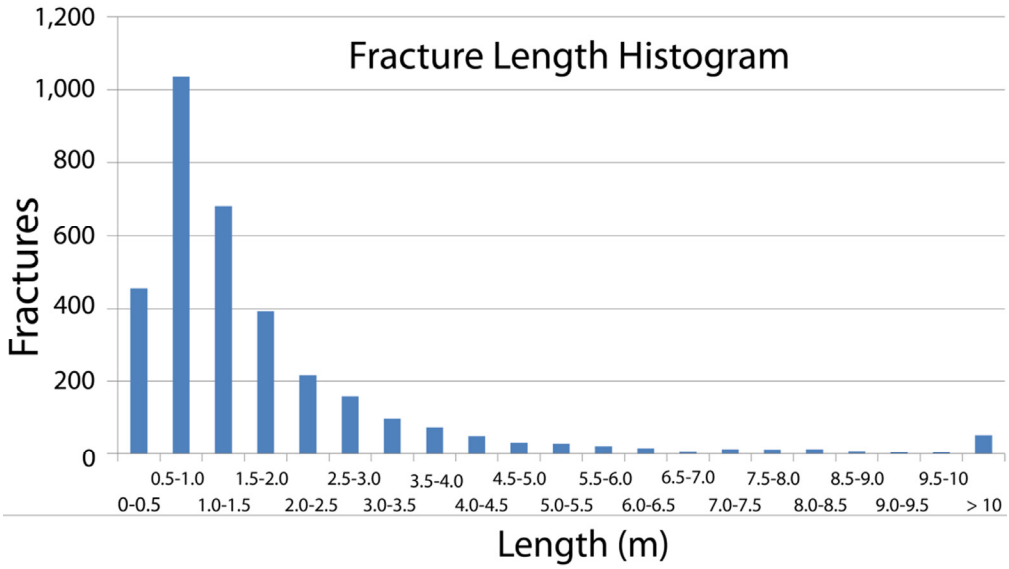

Figure 12. Length histogram for all fractures mapped in Lewis Canyon.

creased weathering along the vertically exposed boundaries, which probably highlights the local natural fracture network more than in areas further away from the boundaries.

Dolomitization, Porosity, and Rock Strength

There are two scales of dolomitization among layers 6–10. Layers 6, 9, and 10 have undergone destructive dolomitization, but still partially show their original depositional fabric and molds of original grains (Fig. 9). Layers 7 and 8 are dolomitized to a greater degree where all depositional fabric is obliterated by replacing dolomite crystals.

Varying degrees of dolomitization and the subsequent differences in crystal size and arrangement are potential factors controlling fracture intensity. Of the three main pavement layers, only layer 8 is dolomitized to a degree where all original depositional fabric is obscured and replaced. In layer 8, the individual dolomite crystals have grown to an average size of ~80–120 microns by replacing original grains and matrix. This process can increase average pore size within the layer and may increase the pore space and improve fluid mobility within rock (Lucia, 1995). While dolomite itself (i.e., mineralogy) is not proposed to control rock strength in Lewis Canyon, a higher porosity in layer 8 is likely associated with its lower UCS. Conversely, layers 9 and 10 have higher UCS values and crystals between ~5–50 microns, but much of their dolomite is replacing the original mud matrix, which creates different textures and lower porosities than the crystalline structures of layers 7 and 8.

The impact dolomitization has on fracture intensity is not well understood. Some studies show dolomitization has a secondary effect on fracture intensity (Wennberg et al., 2006) while others document a positive correlation between dolomite content and fracture intensity (Ortega et al., 2010). However, in Lewis Canyon the degree of dolomitization is shown to be intricately tied to relative fracture intensity and can be interpreted as one control where increased dolomitization correlates to decreased fracture intensity.

In this study all fractures mapped using UAV photos in layer 8 are within 70 m of fault A whereas fractures in layers 9 and 10 are found throughout the entire study area (i.e., up to 140 m away). Layer 8 has the highest porosity, so the complete lack of fractures more than 70 m away from fault A is evidence that faults exert noteworthy control on highly porous (i.e., less competent) layers. Layers 7 and 8 are both crystalline dolomites having similar textures, and as previously discussed, there are only two observed petrologic differences between them. Layer 8 has a larger mean crystal size and a higher porosity than layer 7. Relationships between porosity and rock strength advocated by previous studies are seen to an extent in Lewis Canyon, and the authors posit that porosity is the major control on relative fracture intensity within the observed layers. Compelling to this conclusion is the work of Hatzor et al. (1997), which shows that porosity can be a dominant control on ultimate tensile strength. With 28% porosity, layer 8 has a relatively high compressibility, likely decreasing its UCS. Layer 8 best demonstrates that while the local structural overprint is responsible for fracture development, bed scale lithological differences can control relative fracture intensity.

CONCLUSIONS

Mechanical partitioning is observed as an important characteristic of layered carbonate strata that have fractured and faulted in an oblique-reactivation setting. Fractures in Lewis Canyon are the products of regional oblique reactivation along deep-seated compressional faults. Locally, their spatial intensities and orientations are controlled by slip along nearby surface faults that were created by the same regional tectonics. This process creates a halo of higher fracture intensity around fault A. Fracture intensity decreases away from fault location, but varies between layers. Faults have greater control over the fracturing (i.e., fracture intensity decreases significantly away from the fault) in layers with relatively low unconfined compressive strength (UCS) values, so the rate of intensity change is governed by mechanical properties unique to each layer.

Diagenesis and porosity are identified as controls on fracture development. Specifically, the degree of dolomitization has a direct effect on the mechanical properties of individual layers within Lewis Canyon. A combination of high porosity and a crystalline dolomite fabric in layer 8 is associated with lower UCS and decreased fracture intensity compared to layers 9 and 10, which were subjected to a lesser degree of dolomitization and have lower porosities and higher UCS (Figs. 8 and 9; Table 1).

REFERENCES CITED

Augosta, R., and A. Aydin, 2006, Architecture and deformation mechanism of a basin-bounding normal fault in Mesozoic platform carbonates, central Italy: Journal of Structural Geology, v. 28, p. 1445–1467.

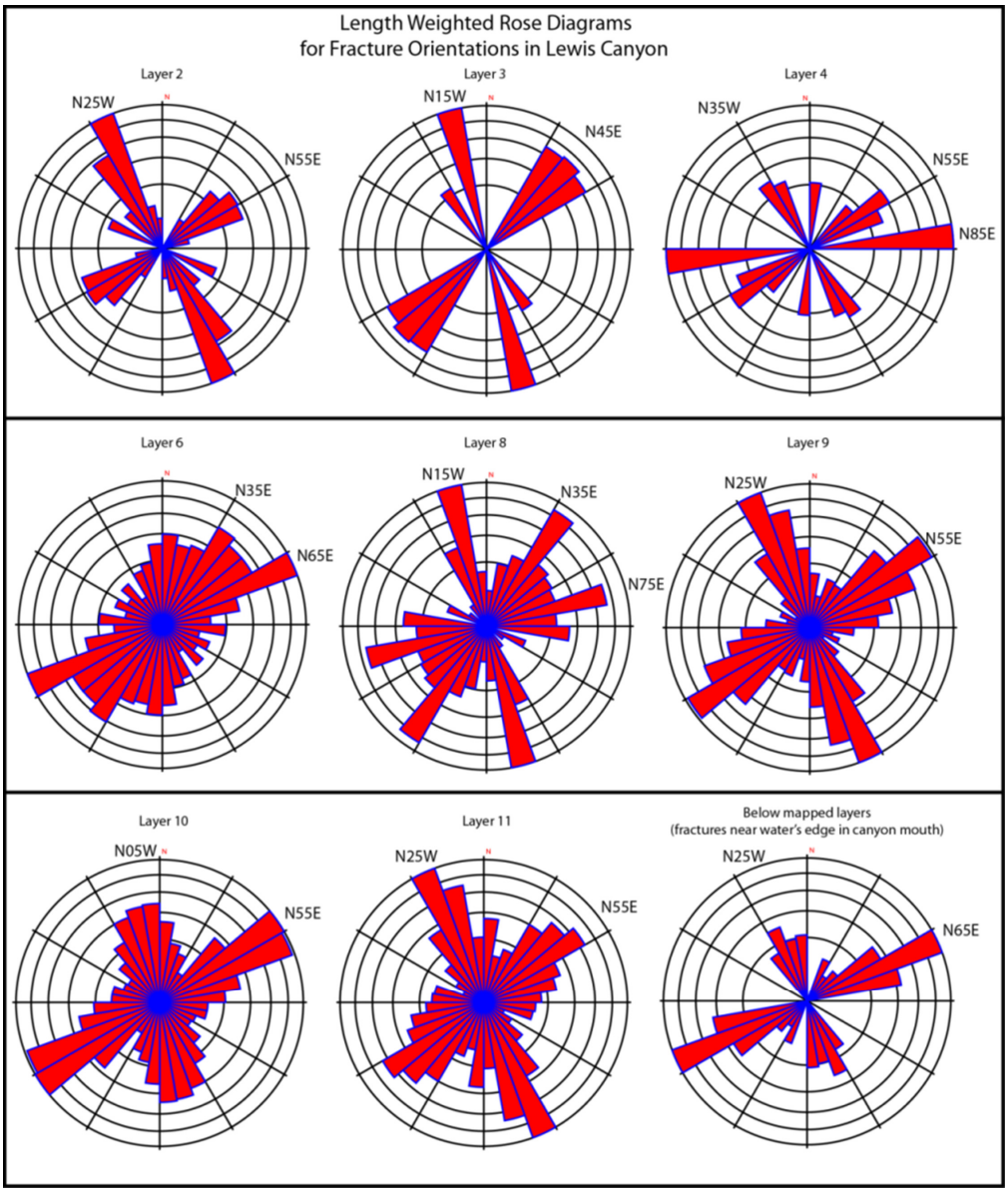

Figure 13. Length-weighted rose diagrams for fractures in layers mapped in Lewis Canyon, including a diagram for fractures mapped below the identified layers.

Burberry, C. M., 2015, Spatial and temporal variation in penetrative strain during compression: Insights from analog models: Lithosphere, v. 7, p. 611–624.

Caine, J. S., J. P. Evans, and C. B. Forster, 1996, Fault zone architecture and permeability structure: Geology, v. 24, p. 1025–1028

Deere, D. U., and R. P. Miller, 1966, Engineering classification and index properties for intact rock: Air Force Systems Command Report AFWL–TR–65–116, Kirtland Air Force Base, New Mexico.

Ewing, T. E., 1990, Tectonic map of Texas: Texas Bureau of Economic Geology, Austin, scale 1:750,000.

Ferrill, D. A., A. P. Morris, R. N. McGinnis, K. J. Smart, and W. C. Ward, 2011, Fault zone deformation and displacement partitioning in mechanically layered carbonates: The Hidden Valley Fault, Central Texas: American Association of Petroleum Geologists Bulletin, v. 95, p. 1383–1397.

Flawn, P. T., A. Goldstein Jr., P. B. King, and C. E. Weaver, 1961, The Ouachita System: Texas Bureau of Economic Geology Publication 6120, 401 p.

Freeman, V. L., 1961, Contact of Boquillas flags and Austin Chalk in Val Verde and Terrell counties, Texas: American Association of Petroleum Geologists Bulletin, v. 45, p. 105–107.

Goldhammer, R. K., and C. A. Johnson, 2001, Middle Jurassic–Upper Cretaceous paleogeographic evolution and sequence-stratigraphic framework of the northwest Gulf of Mexico rim, *in* C. Bartolini, R. T. Buffler, and A. Cantu-Chapa, eds., The western Gulf of Mexico Basin: Tectonics, sedimentary basins, and petroleum systems: American Association of Petroleum Geologists Memoir 75, Tulsa, Oklahoma, p. 45–81.

Groshong, R. H., 1975, Strain, fractures, and pressure solution in natural single-layer folds: Geological Society of America Bulletin, v. 86, p. 1363–1376.

Hatzor, Y. H., A. Zur, and Y. Mimran, 1997, Microstructure effects on microcracking and brittle failure of dolomites: Tectonophysics, v. 281, p. 141–161.

Hogan, J. P., and W. M. Dunne, 2001, Calculation of shortening due to outcrop-scale deformation and its relation to regional deformation patterns: Journal of Structural Geology, v. 23, p. 1507–1529.

Kastning, E. H., 1983, Relict caves as evidence of landscape and aquifer evolution in a deeply dissected carbonate terrain: southwest Edwards Plateau, Texas, U.S.A.: Journal of Hydrology, v. 61, p. 89–112

Kerans, C., and R. G. Loucks, 2002, Stratigraphic setting and controls on occurrence of high-energy carbonate beach deposits: Lower Cretaceous of the Gulf of Mexico: Gulf Coast Association of Geological Societies Transactions, v. 52, p. 517–526.

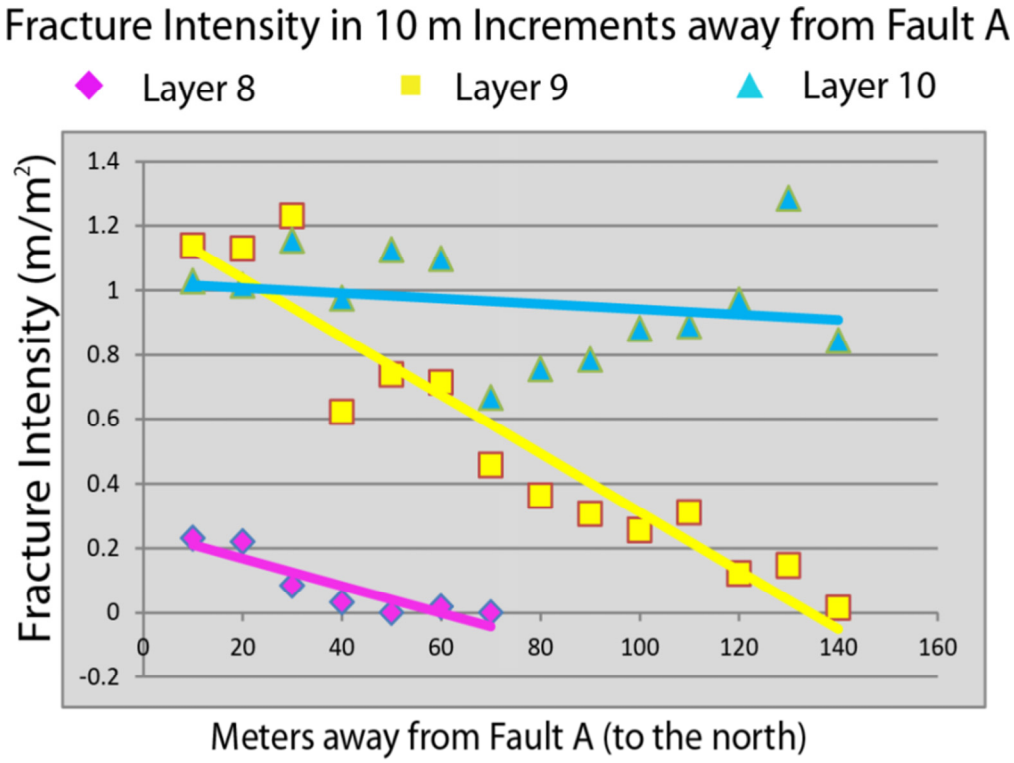

Figure 14. Graph of fracture intensities calculated in 10 m bands away from fault A. Layers 8 and 9 show strong decreasing linear trends and layer 10 shows a weak decreasing linear trend.

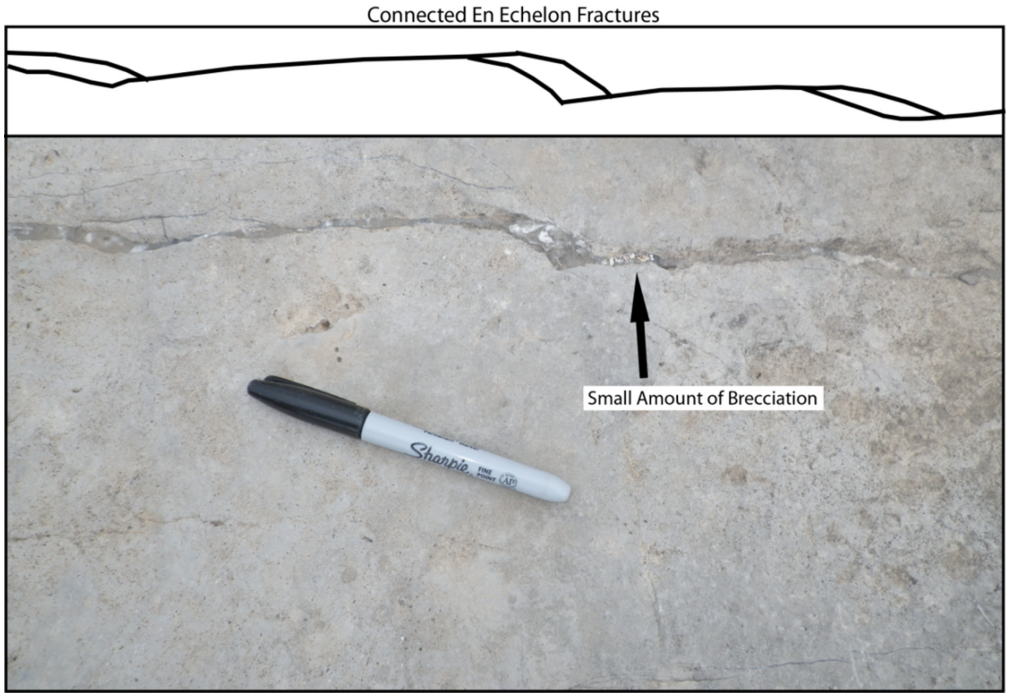

Figure 15. Outcrop photo and diagram of fracture linkage. Fracture width is thickest at the linkage step where a small amount of brecciation has occurred.

Kerans, C., R. Aisner, and C. K. Zahm, 2010, The Mural Limestone of Arizona: An outcrop analog for the Aptian-Albian patch-reef reservoirs of the Maverick Basin: Texas Bureau of Economic Geology Reservoir Characterization Research Laboratory Field Trip Guidebook, Austin, October 20–22, 54 p.

Lucia, F. J., 1995, Rock-fabric/petrophysical classification of carbonate pore space for reservoir characterization: American Association of Petroleum Geologists Bulletin, v. 79, p. 1275–1300.

McGinnis, R. N., D. A. Ferrill, K. J. Smart, A. P. Morris, C. Higuera-Diaz, and D. Prawica, 2015, Pitfalls of using entrenched fracture relationships: Fractures in bedded carbonates of the Hidden Valley Fault Zone, Canyon Lake Gorge, Comal County, Texas: American Association of Petroleum Geologists Bulletin, v. 99, p. 2221–2245.

Mitra, G., and W. A. Yonkee, 1985, Relationship of spaced cleavage to folds and thrusts in the Idaho-Utah-Wyoming Thrust Belt: Journal of Structural Geology, v. 7, p. 361–373.

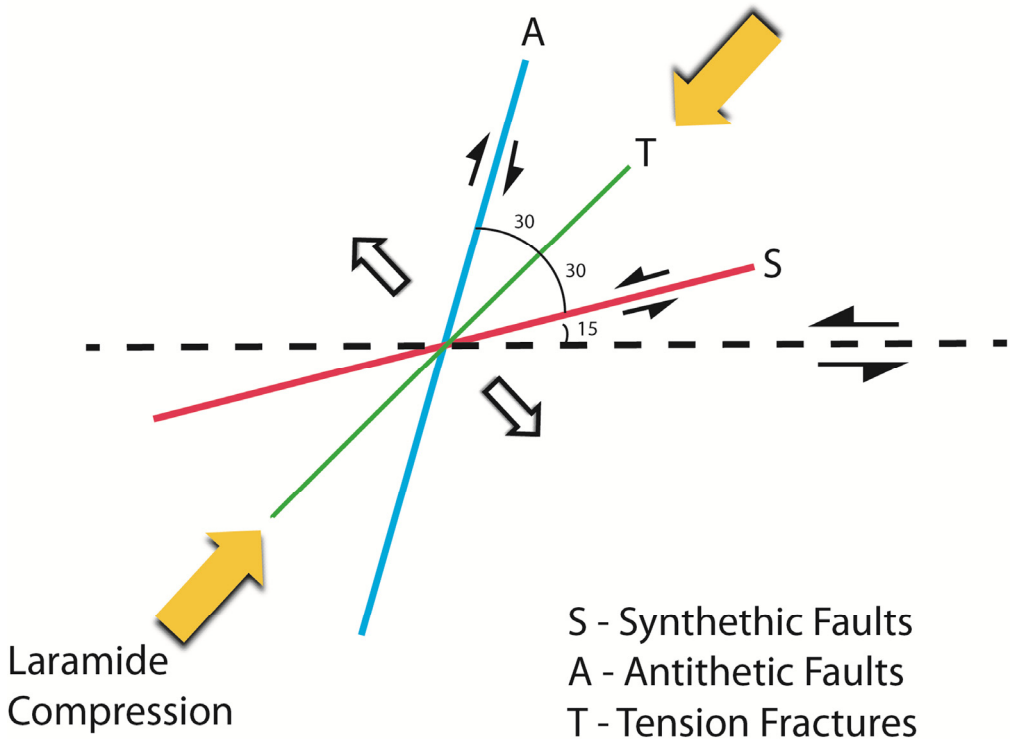

Figure 16. Predicted fault orientations created during oblique shear (modified after Wilcox et al., 1983; Woodcock and Schubert, 1994). Black dotted line represents the pre-existing structure reactivated obliquely with a sense of left-lateral slip.

Moody, J. D., and M. J. Hill, 1956, Wrench-fault tectonics: Geological Society of America Bulletin, v. 67, p. 1207–1246.

Nicholas, R. L., and R. A. Rozendal, 1975, Subsurface positive elements within Ouachita Foldbelt in Texas and their relation to Paleozoic cratonic margins: American Association of Petroleum Geologists Bulletin, v. 59, p. 193–216.

Ortega, O. J., J. F. W. Gale, and R. Marrett, 2010, Quantifying diagenetic and stratigraphic controls on fracture intensity in platform carbonates: An example from the Sierra Madre Oriental, northeast Mexico: Journal of Structural Geology, v. 32, p. 1943–1959.

Poole, R. W., and I. W. Farmer, 1980, Consistency and repeatability of Schmidt hammer rebound data during field testing: International Journal of Rock Mechanics and Mining Science and Geomechanics Abstracts, v. 17, p. 167–171.

Riedel, W., 1929, *Zur mechanik geologischer brucherscheinungen*: *Zentralblatt für Mineralogie, Geologie und Paläontologie* 929B, p. 354–368.

Sellards, E. H., W. S. Adkins, and F. B. Plummer, 1933, The geology of Texas, v. 1: Stratigraphy: Texas Bureau of Economic Geology Bulletin 3232, Austin, 1030 p.

Scott, R. J., 2004, The Maverick Basin: New technology—New success: Gulf Coast Association of Geological Societies Transactions, v. 54, p. 603–620.

Smith, G. A., 2013, Fault and fracture systems related to reactivation of pre-existing structural elements, Devils River Uplift and Maverick Basin, Texas: Master's Thesis, University of Texas at Austin, 194 p.

Tchalenko, J., and N. Ambraseys, 1970, Similarities between shear zones of different magnitudes: Geological Society of America Bulletin, v. 81, p. 1625–1640.

Webster, R. E., 1980, Structural analysis of Devils River Uplift–Southern Val Verde Basin, southwest Texas: American Association of Petroleum Geologists Bulletin, v. 64, p. 221–241.

Wennberg, O. P., T. Svana, M. Azizzahed, A. M. M. Aqrawi, P. Brockbank, K. B. Lyslo, and S. Ogilvie, 2006, Fracture intensity vs. mechanical stratigraphy, in platform top carbonates: The Aquitanian of the Asmari Formation, Khaviz Anticline, Zagros, SW Iran: Petroleum Geoscience, v. 12, p. 235–246.

Wilcox, R. E., T. P. Harding, and D. R. Seely, 1973, Basic wrench tectonics: American Association of Petroleum Geologists Bulletin, v. 57, p. 74–96.

Wojtal, S., 1989, Measuring displacement gradients and strains in faulted rocks: Journal of Structural Geology, v. 11, p. 669–678.

Woodcock, N. H., and C. Schubert, 1994, Continental strike-slip tectonics *in* P. L. Hancock, ed., Continental deformation: Pergamon Press, New York, New York, p. 251–263.

Zahm, C. K., and C. Kerans, 2007, Painted Canyon facies-bound within the Albian 19 HST, *in* C. Kerans, J. A. Bellian, R. M. Phelps, and C. Zahm, eds., Cretaceous reservoir heterogeneity styles: Facies to fractures: Texas Bureau of Economic Geology Reservoir Characterization Research Laboratory Field Trip Guidebook, Austin, October 9–12, p. 102–104.

Zahm, C., and C. Kerans, 2010, Small faults, big damage zones: An example of fault-related fractures and dissolution collapse in a ramp crest carbonate system, lower Pecos River Canyon, Texas: American Association of Petroleum Geologists Search and Discovery Article 50341, Tulsa, Oklahoma, 42 p. <http://www.searchanddiscovery.com/pdfz/documents/2010/50341zahm/ndx_zahm.pdf.html> Last Accessed August 15, 2016.

Zahm, C. K., and C. Kerans, 2012, The use of stratigraphic architecture and rock strength for improved carbonate fracture reservoir modeling—Examples from outcrop analogs and subsurface reservoirs: American Association of Petroleum Geologists Search and Discovery Article 120097, Tulsa, Oklahoma, 13 p., <http://www.searchanddiscovery.com/documents/2012/120097zahm/ndx_zahm.pdf> Last Accessed August 15, 2016.

Zahm, C. K., and M. Enderlin, 2010, Characterization of rock strength in Cretaceous strata along the Stuart City Trend, Texas: Gulf Coast Association of Geological Societies Transactions, v. 60, p. 693–702.

Zahm, C. K., L. C. Zahm, and J. A. Bellian, 2010. Integrated fracture prediction using sequence stratigraphy within a carbonate fault damage zone, Texas, USA: Journal of Structural Geology, v. 32, p. 1363–1374.

Zahm, C. K., 2013, Use of unmanned aerial vehicles (UAVs) for characterization of embryonic fractures along the western shoreline of West Caicos platform margin, Turks and Caicos, West Indies: Texas Bureau of Economic Geology Reservoir Characterization Research Laboratory Annual Meeting, Austin, Oct. 22.